INNOVATION FOREVER
Open Access

Innovation Discovery
ISSN 2959-5150 (Online)

Research Article

He-Ne Laser-Driven Transformation of SeTeSb Glass: A Pathway to Tunable Electrical and Optical Properties

Namrata Chandel[1], Neeraj Mehta[1*]

[1]*Physics Department, Banaras Hindu University, Varanasi, India*

[*]***Correspondence to: Neeraj Mehta, PhD, Professor,*** *Physics Department, Banaras Hindu University, Ajagara, Varanasi, Uttar Pradesh, 221005, India; Email: drnmehta@bhu.ac.in*

Abstract

A simple laser-assisted approach was employed to tailor the structural, electrical and optical properties of an amorphous $Se_{80}Te_{10}Sb_{10}$ alloy. Controlled He-Ne laser irradiation induced partial crystallization and grain growth, resulting in significant modifications of the dielectric, thermal and optical characteristics. The present study demonstrates laser-induced structural evolution accompanied by measurable changes in thermal stability, electrical transport and optical response. The structural evolution and associated changes in the physical properties of the amorphous $Se_{80}Te_{10}Sb_{10}$ alloy following He-Ne laser irradiation were systematically evaluated through different characterization techniques. The observed laser-induced structural evolution demonstrates that controlled optical irradiation offers an effective route to tune the functional properties of Se-Te-Sb glasses for future photonic and phase-change applications.

Keywords: amorphous, alloys, glass transition, optical bandgap

Received: December 15, 2025
Revised: July 10, 2026
Accepted: August 28, 2026
Published: September 9, 2026

Copyright © 2026 The Author(s). Published by Innovation Forever Publishing Group Limited. This open-access article is licensed under a Creative Commons Attribution 4.0 International License (https://creativecommons.org/licenses/by/4.0), which permits unrestricted use, sharing, adaptation, distribution, and reproduction in any medium, provided the original work is properly cited.

Citation: Chandel N, Mehta N. He-Ne Laser-Driven Transformation of SeTeSb Glass: A Pathway to Tunable Electrical and Optical Properties. *Innov Discov*, 2026; 3(3): 13.

1 INTRODUCTION

Chalcogenide-based alloys are multifunctional materials since their structural, electrical, optical and thermal properties can be tailored over a wide range through compositional design. This versatility has led to their extensive use in photovoltaic technologies, phase-change memories, thermoelectric devices, infrared optics and other optoelectronic applications. Traditionally, these properties have been modified by incorporating suitable dopants into the host matrix to alter its electronic structure and local atomic environment. More recently, interest has shifted toward post-synthesis approaches in which external stimuli, such as laser irradiation, electric fields, or energetic radiation, are employed to engineer material properties without altering the overall chemical composition of the material[1-4]. In addition to compositional modification, irradiation-based techniques have emerged as effective post-synthesis approaches for engineering the properties of chalcogenide materials. Exposure to energetic particles or electromagnetic radiation can alter the local atomic arrangement, defect distribution and crystallization behaviour without changing the overall composition of the material. Previous investigations have demonstrated that the physical properties of these materials are significantly sensitive to external irradiation[5-8]. Among these approaches, laser processing is particularly attractive because it offers precise spatial control, rapid processing and localized energy delivery, enabling selective modification of the material with minimal influence on the surrounding region.

The interaction of laser radiation with amorphous chalcogenide glasses results in electronic excitation followed by bond rearrangement, structural relaxation and, under appropriate irradiation conditions, partial crystallization of the amorphous network. Unlike

conventional oxide glasses, chalcogenide glasses exhibit pronounced photo-induced effects owing to their flexible covalent network and the presence of lone-pair electrons associated with chalcogen atoms. These characteristics make them highly responsive to optical irradiation even at relatively low laser powers. Consequently, laser-induced structural modification has become an important strategy for tuning the physical properties of chalcogenide-based alloys and for developing applications in optical recording, phase-change memories, integrated photonics and programmable photonic devices[9-14]. Laser irradiation modifies amorphous chalcogenides through localized photon absorption, electronic excitation and subsequent structural relaxation. When the absorbed photon energy exceeds the activation energy associated with weak heteropolar bonds, bond rearrangement occurs, leading to nucleation and growth of crystalline regions. Unlike conventional furnace annealing, laser processing offers spatially selective energy delivery with minimal thermal damage, making it attractive for optical memory, integrated photonics and programmable electronic materials. Depending on the laser wavelength, irradiation time and power density, localized photon absorption can induce bond switching, structural relaxation, defect redistribution and controlled crystallization without significantly affecting the surrounding material. Such laser-induced modifications provide precise spatial control and have attracted considerable attention for the fabrication of integrated photonic circuits and optical memories. Recent studies on Ge-Sb-Te, Sb-Se, and related chalcogenide systems further demonstrate that laser irradiation can efficiently manipulate crystallization kinetics and optical contrast, enabling reversible tuning of material properties for next-generation photonic applications[15,16].

The microscopic processes responsible for laser-induced structural modification in chalcogenide glasses remain an active area of investigation. It is generally accepted that optical excitation promotes electrons from localized tail states into higher-energy states, initiating bond rearrangement and atomic redistribution within the amorphous network. These electronic and atomic processes modify the populations of coordination defects and metastable structural configurations, leading to measurable changes in the material's structural, electrical, and optical properties[15,16]. Since defect formation and structural relaxation are closely coupled in amorphous chalcogenides, both are considered to play key roles in the photoinduced evolution of their physical characteristics[17,18]. Recent experimental and theoretical studies have shown that photo-induced crystallization in chalcogenide glasses is governed by electronic excitation followed by atomic rearrangement within the amorphous network. The formation of transient defect states weakens relatively unstable bonds and lowers the activation barrier for nucleation, thereby promoting the growth of nanocrystalline regions under continuous optical irradiation. The extent of crystallization strongly depends on the local network connectivity and chemical composition, making Se-based chalcogenide glasses attractive model systems for investigating light-induced structural transformations[10-14].

The relatively low electrical conductivity of undoped chalcogenide glasses limits their performance in many electronic and optoelectronic applications. Consequently, compositional modification through suitable alloying elements has become an effective strategy for tailoring their electrical, optical and thermal characteristics. Among the various additives investigated, antimony has attracted considerable interest because it enhances thermal stability, influences crystallization behaviour and modifies the electronic structure of Se-based glassy networks[19-21]. Antimony-containing chalcogenides are also of considerable technological importance due to their applications in infrared optics, thermoelectric energy conversion, optoelectronic devices, and phase-change memory technologies. In addition, binary compounds such as Sb_2Te_3 exhibit topological insulating behaviour arising from strong spin-orbit coupling, whereas Sb_2Se_3 possesses distinct semiconducting characteristics with comparatively weaker topological features. Incorporation of Sb into Se-Te glasses therefore provides an effective means of tuning the local atomic arrangement and electronic properties while simultaneously improving the functionality of the host material. Consequently, Se-Te-Sb alloys represent an attractive class of composition-dependent chalcogenide semiconductors for investigating laser-induced structural and property modifications. Currently, numerous studies focus on the fabrication of Sb_2Se_3[22-25] and Sb_2Te_3[26-28] alloys using various methods. However, only a few studies have addressed the problem of SeTeSb-based alloys across different compositions[3,29]. Although laser processing has been widely explored for thin-film chalcogenides, systematic studies on bulk Se-Te-Sb glasses remain scarce. The present investigation therefore aims to establish the relationship between laser-induced structural evolution and the resulting electrical, dielectric, thermal and optical properties of bulk $Se_{80}Te_{10}Sb_{10}$ glass. We have studied the influence of laser irradiation on the structural and functional characteristics of amorphous $Se_{80}Te_{10}Sb_{10}$ glass. Following a controlled irradiation period of 15min, comprehensive characterization was conducted to evaluate changes in morphology, crystallization behaviour, electrical transport, dielectric response, hardness, and optical properties.

2 MATERIALS AND METHODS

The source material, a-$Se_{80}Te_{10}Sb_{10}$ alloy, was synthesized using a well-established route: rapid solidification from the melt[29]. The prepared sample was irradiated with a He-Ne laser at 632.8nm and an output power of 2mW. The irradiation was carried out for 15min to investigate laser-induced modifications in the

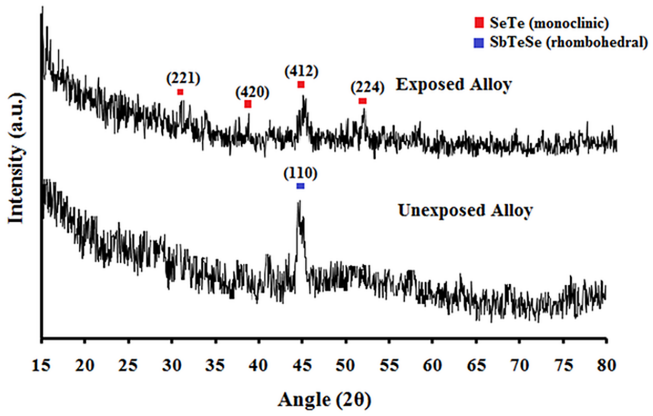

Figure 1. XRD Patterns of As-Synthesized and Laser-Exposed a-$Se_{80}Te_{10}Sb_{10}$ Alloys.

specimen's physical properties.

The diffraction patterns were recorded using a Shimadzu PW1710 X-ray diffractometer (Japan) equipped with Cu K_α radiation (λ=1.5405Å). The instrument was operated at an accelerating voltage of 40kV and a tube current of 30mA. Morphological and microstructural features were further investigated using a transmission electron microscope[Model: FEI Tecnai 20 G2] and a scanning electron microscope[Model: JEOL 840A]. The thermal behaviour was investigated under non-isothermal conditions using TA Instruments, Model Q20 MDSC. Powdered specimens weighing approximately 5-10mg were sealed in aluminium pans and heated at a constant heating rate under a flowing nitrogen atmosphere (50mL/min). The DSC instrument provided a heat-flow resolution of ±0.01mW, while the temperature measurement accuracy was ±0.1K. The capacitance and dissipation-factor measurements were performed under vacuum of 10^{-3} Torr with a rotary pump. Wayne Kerr 4255 digital LCR meter was used for this purpose. The mechanical hardness of the samples was evaluated after polishing the pellet surfaces using an automated digital Vickers microhardness tester (Vaiseshika Electron Devices, Model DHV-1000).

The optical characterization was performed using a UV-Vis spectrophotometer (Shimadzu UV-1601, a computerized spectrophotometer for UV/VIS/NIR). The Raman spectrum was recorded using a micro-Raman spectrophotometer with 514.5nm excitation, a 2,400 lines/mm grating, and a Peltier-cooled CCD. Infrared spectra for the glass powder were recorded using a Varian 3100 FT-IR spectrometer through KBr disks.

3 RESULTS AND DISCUSSION

3.1 Structural Analysis

Figure 1 shows the X-ray diffraction (XRD) of unexposed and exposed a-$Se_{80}Te_{10}Sb_{10}$ alloys. The absence of sharp peaks in the XRD pattern of the as-synthesized Se80Te10Sb10 alloy confirms its amorphous nature; however, only one small-intensity peak is observed at ~45^0. This peak has been indexed by the SbTeSe (rhombohedral) phase. The cell parameters are *a*=4.18Å and *c*=29.78Å. The average coherent crystallite size *D* of unexposed a-$Se_{80}Te_{10}Sb_{10}$ alloy has been calculated using the Equation[30]:

$$D = \frac{0.91\lambda}{\beta \cos\theta} \quad (1)$$

Here, λ and θ are the wavelength and the Bragg angle; while β is the full width at half maximum. From the powder XRD analysis of the present alloys, the average grain size of the unexposed a-$Se_{80}Te_{10}Sb_{10}$ alloy is approximately 21nm. A similar procedure was followed to determine the grain size of the exposed alloy, which was approximately 24.4nm, indicating a notable change. It should be noted that the crystallite size calculated from the Debye-Scherrer equation represents the coherent diffraction domain size rather than the physical particle size observed by SEM or TEM. Therefore, SEM and TEM observations are employed only as qualitative confirmation of grain coarsening induced by laser irradiation. The diffraction peaks observed after laser irradiation indicate partial crystallization of the initially amorphous $Se_{80}Te_{10}Sb_{10}$ matrix. Rather than representing a direct crystallographic transformation from the rhombohedral SbTeSe phase to the monoclinic SeTe phase, the laser irradiation promotes atomic rearrangement within the amorphous network, leading to preferential nucleation and growth of thermodynamically stable SeTe crystallites embedded in the residual amorphous matrix. The observed increase in crystallite size from approximately 21 to 24.4nm indicates that prolonged continuous-wave laser irradiation supplies sufficient energy for localized atomic diffusion and crystal growth. Similar laser-assisted grain growth has recently been reported for several chalcogenide phase-change materials, where localized structural relaxation precedes nucleation and crystallization. The present observations therefore agree well with the current understanding of photo-induced crystallization in selenium-based chalcogenides[31,32].

Other microstructural parameters, such as strain and dislocation density, have been calculated using the following formulae:

$$Strain = \frac{\beta \cos\theta}{4} \quad (2)$$

$$Dislocationdensity = \frac{1}{D^2} \quad (3)$$

The calculated micro-strain and dislocation density are employed only as comparative structural parameters to evaluate the influence of laser irradiation. Since both samples were analyzed under identical instrumental conditions, relative changes due to peak broadening can be reliably interpreted despite the inherent limitations of the Scherrer approach. The values of the above-

Table 1. Microstructural Parameters of a-$Se_{80}Te_{10}Sb_{10}$ Alloy before and after Laser Exposure

Sample	Grain Size (D) (nm)	δ (×10^{15}lines/m^{-2})	Strain (×10^{-3})
Unexposed a-$Se_{80}Te_{10}Sb_{10}$ alloy	21.0	2.27	1.67
Exposed a-$Se_{80}Te_{10}Sb_{10}$ alloy	24.4	1.68	1.50

Table 2. Different Structural Parameters in Exposed Sample of a-$Se_{80}Te_{10}Sb_{10}$ Alloy

2 (degree)	d (Å) values		FWHM (2θ)
	Experimental	Theoretical	
30.5	2.97	2.93	0.2952
40.7	2.22	2.21	0.3936
44.6	2.03	2.03	0.4920
51.3	1.78	1.78	0.2952

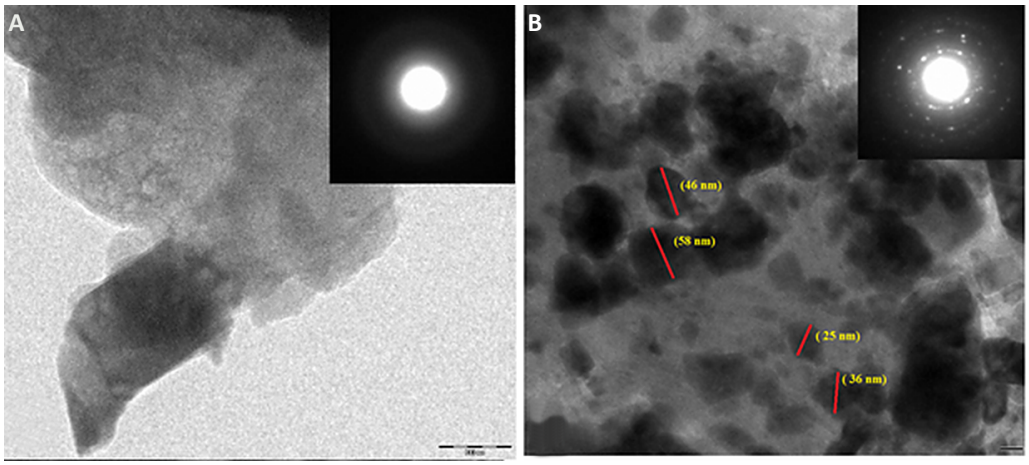

Figure 2. TEM Images of (A) As-Prepared and (B) Laser-Exposed a-$Se_{80}Te_{10}Sb_{10}$ Alloy.

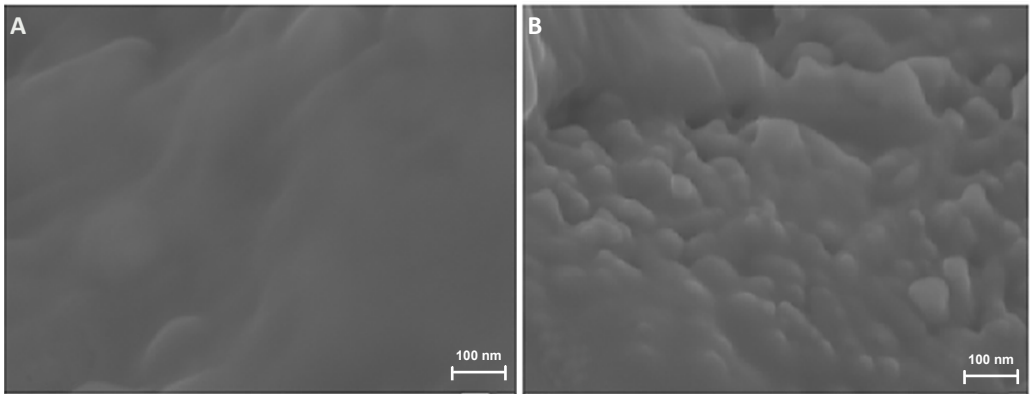

Figure 3. SEM Images of (A) As-Prepared and (B) Laser-Exposed $Se_{80}Te_{10}Sb_{10}$ Alloys.

mentioned structural parameters are listed in Table 1. The corresponding microstructural parameters are given in Table 2. The TEM image of the unexposed a-$Se_{80}Te_{10}Sb_{10}$ alloy (Figure 2A) reveals a relatively flat morphology with transparent layers stacked one over another. The silk-like texture, along with wrinkles and folded regions, is characteristic of the parent alloy's predominantly amorphous structure. The silk-like and restacked parts are visible. Wrinkles and folds are observed on the surface and at the edges of the structure. As shown in Figure 2B, laser irradiation leads to the dispersion and aggregation of particles. Upon zooming in on the image, the round particles are visible. The corresponding electron diffraction patterns are shown in the inset, respectively.

The influence of laser radiation on the parent alloy, a-$Se_{80}Te_{10}Sb_{10}$, was examined using SEM. From these figures, some crystallite-like bodies are detected in the amorphous matrix before laser irradiation. The average particle size was 40nm (see Figure 3A), whereas irradiation of the parent alloy yielded larger particles and agglomerates (see Figure 3B). The laser-exposed alloy

Table 3. Kinetic Parameters T_g, T_c, T_m, H_r, and T_{rg} of a-$Se_{80}Te_{10}Sb_{10}$ Alloy before and after Laser Exposure

Sample	T_g (K)	T_c (K)	T_m (K)	H_r	T_{rg}
Unexposed a-$Se_{80}Te_{10}Sb_{10}$ alloy	339	390	515	0.41	0.66
Exposed a-$Se_{80}Te_{10}Sb_{10}$ alloy	343	384	516	0.31	0.66

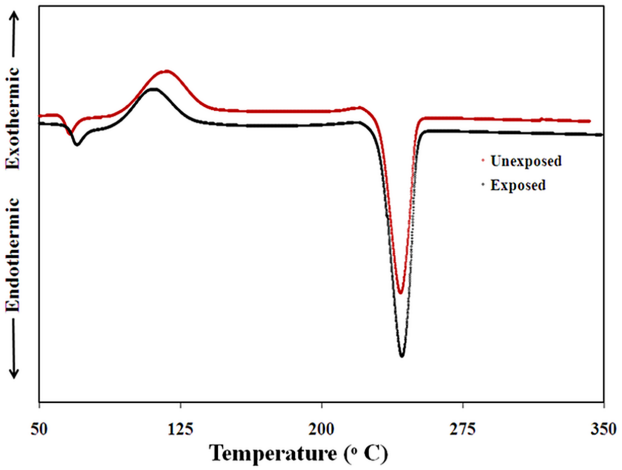

Figure 4. DSC Scans of the Unexposed and Exposed Samples of a- $Se_{80}Te_{10}Sb_{10}$ Alloy Recorded from 50 to 350°C.

exhibits larger grains than the unexposed sample, as confirmed by XRD and TEM results.

Further evidence of laser-induced structural evolution is provided by TEM and SEM observations. The TEM micrographs reveal noticeable changes in particle morphology after laser irradiation, with the exposed sample exhibiting larger and more aggregated particles than the unexposed alloy. In addition, the corresponding selected-area electron diffraction (SAED) pattern of the laser-exposed sample exhibits more distinct diffraction rings, indicating increased crystalline ordering relative to the parent alloy's predominantly amorphous nature. The SEM micrographs further demonstrate grain coarsening and particle agglomeration following laser irradiation. These observations are in good agreement with the XRD results, confirming that He-Ne laser irradiation promotes partial crystallization and grain growth in the amorphous $Se_{80}Te_{10}Sb_{10}$ matrix.

3.2 Thermal Characterization

In a DSC scan, the crystallization (T_c) and glass transition (T_g) temperatures are indicated by temperature peaks, analogous to exothermic and endothermic peaks, respectively, due to abrupt changes in specific heat. As shown in Figure 4, T_g increases after laser exposure due to increased orderliness and decreased entropy in these glasses, while T_c decreases. The most pronounced modification occurs below approximately 150°C, which corresponds to the glass transition region, where structural relaxation dominates. Laser irradiation primarily alters short-range atomic ordering without changing the overall chemical composition. Consequently, only minor changes are observed in the melting temperature, whereas T_g and T_c exhibit noticeable shifts. The values of T_c, T_g, T_m are listed in Table 3. From this table, we observe a remarkable change in the values of T_g and T_c as a consequence of the irradiation effect.

Kauzmann[33] proposed that the ratio of the glass transition temperature to the melting temperature, $T_{rg}=(T_g/T_m)$, remains close to 2/3 for many glass-forming systems. This empirical relationship, known as the *two-thirds rule*, provides a useful criterion for evaluating glass-forming ability. The calculated values of T_{rg} for the present alloys, listed in Table 3, are in good agreement with this relationship. Another parameter frequently employed to assess glass-forming ability is the Hruby parameter (H_r)[34], expressed as (T_c-T_g) to (T_m-T_c). A larger value of H_r generally indicates greater resistance to crystallization and, consequently, improved glass-forming tendency (Table 3).

3.3 Electrical Transport Properties

The frequency-dependent a.c. electrical conductivity, $\sigma_{ac}(\omega)$, follows the empirical power-law relationship[35]:

$$\sigma_{ac} = \sigma_{tot} - \sigma_{dc} = A\omega^s \quad (4)$$

Since the measured dc conductivity (σ_{dc}) is several orders of magnitude smaller than the total conductivity in the investigated frequency range, its contribution is negligible. Consequently, the measured conductivity is dominated by the ac component (σ_{ac}), and Equation (4) can therefore be simplified accordingly. The variation of σ_{ac} with frequency for the unexposed and laser-exposed $Se_{80}Te_{10}Sb_{10}$ alloys was examined over the 0.5-100kHz range within the glass-transition region. As illustrated in Figure 5, the ac conductivity increases continuously with increasing frequency for both samples. At lower frequencies, the unexposed alloy exhibits comparatively higher conductivity, whereas above approximately 10 kHz the laser-exposed sample becomes more conducting. This crossover behaviour suggests that laser irradiation modifies the distribution of localized states and the hopping probability of charge carriers.

The frequency exponent (s) was obtained from the slopes of the linear plots shown in Figure 5, and their temperature dependence is presented in Figure 6. For both samples, the exponent lies between 0.35 and 0.65 and decreases monotonically as temperature increases. The observed behaviour of $s(T)$ provides useful insight into the dominant charge transport mechanism. Several theoretical models have been proposed to explain

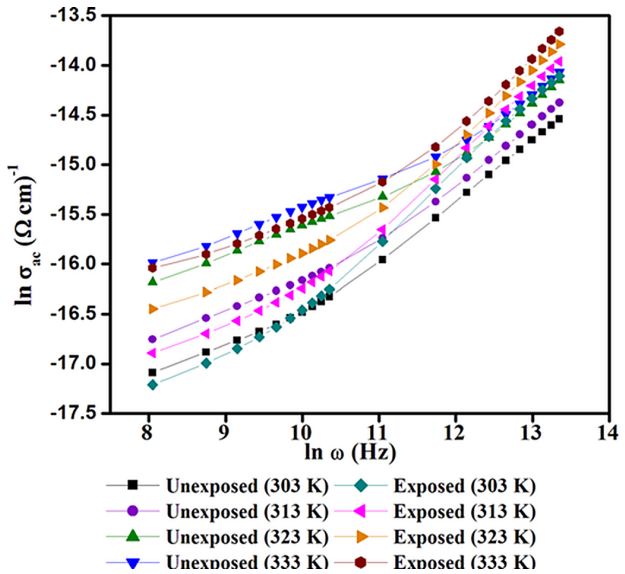

Figure 5. Plots of lnσ_{ac} versus lnω at Different Temperatures for Unexposed and Exposed a- $Se_{80}Te_{10}Sb_{10}$ Alloy.

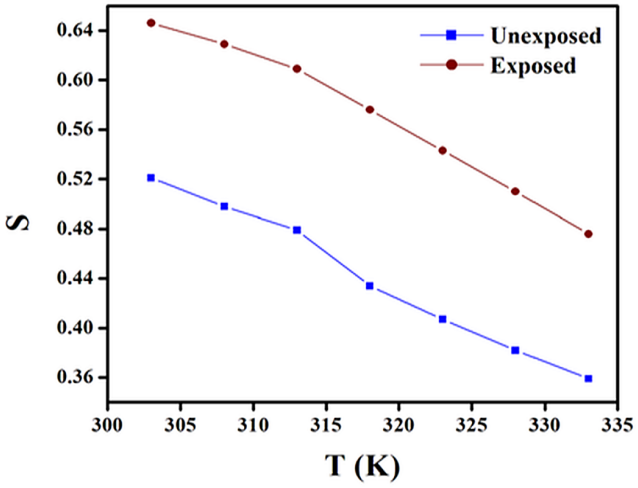

Figure 6. Temperature Dependence of Parameter "*S*" for Unexposed and Laser-exposed Samples of a $Se_{80}Te_{10}Sb_{10}$ Alloy.

ac conduction in disordered materials, including the quantum-mechanical tunnelling (QMT), non-overlapping small-polaron tunnelling (NSPT), large-polaron tunnelling (LPT), and correlated barrier hopping (CBH) models[36]. Each model predicts a characteristic variation of the frequency exponent with temperature. In the QMT model, *s* remains nearly independent of temperature, whereas the NSPT model predicts an increase in s as temperature increases. The LPT model suggests a non-monotonic variation of s, while the CBH model predicts a gradual decrease in *s* as temperature rises. The experimentally observed decrease in frequency exponent is therefore consistent with the CBH model.

In this case, s in terms of the characteristic relaxation time τ_0 and barrier height W_m is given by Elliott[37]:

$$s = 1 - \frac{6k_BT}{W_m + [k_BT\ ln(\omega\tau_0)]} \quad (5)$$

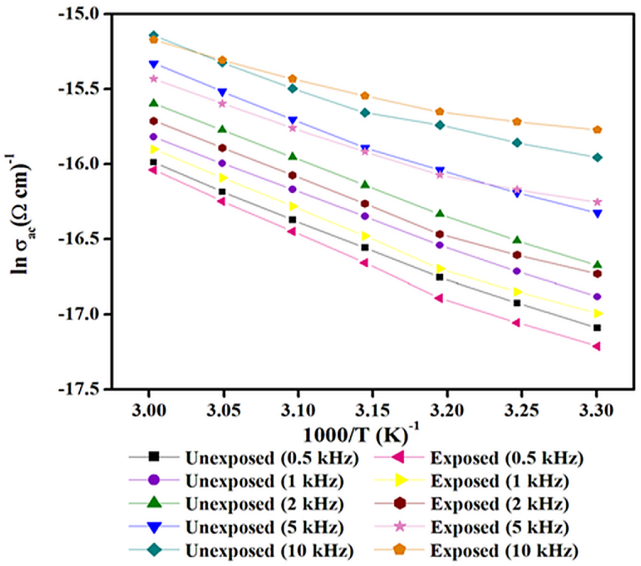

Figure 7. Plots of lnσ_{ac} Against 1000/T at Different Frequencies for Unexposed and Laser Exposed Samples of a-$Se_{80}Te_{10}Sb_{10}$ Alloy.

Figure 7 illustrates the temperature dependence of the ac conductivity for the unexposed and laser-exposed $Se_{80}Te_{10}Sb_{10}$ alloys at different measuring frequencies. In the temperature interval 300-335K, the plots of log σ_{ac} versus 1000/T exhibit approximately linear behaviour, indicating that charge transport is governed by a thermally activated process in this region. The corresponding activation energies were determined from the slopes of the linear fits and are summarized in Table 4. The observed increase in σ_{ac} with temperature is satisfactorily described by the Arrhenius expression in the intermediate temperature range:

$$\sigma_{ac} = (\sigma_0)_{ac} exp\left(\frac{-E_{ac}}{K_BT}\right) \quad (6)$$

Table 4 indicates that the activation energy E_{ac} reduces as frequency increases. From this table, it is clear that the variation of the activation energy of thermally activated a.c. conduction with frequency is remarkable. The laser appears to reconfigure the localized states in the a-$Se_{80}Te_{10}Sb_{10}$ alloy, resulting in a significant decrease in E_{ac}.

The simultaneous hopping of a charge-carrier pair (bipolaron hopping) between oppositely charged defect centres, D^+ and D^-, is the dominant conduction mechanism in the CBH model. The potential barrier encountered during the hopping process originates from the Coulombic interaction between these defect centres and depends on their spatial separation. Based on this mechanism, the frequency-dependent ac conductivity for bipolaron hopping between correlated D^+ and D^-defect pairs is expressed as:

$$\sigma_{ac}(\omega) = \frac{1}{3}\pi^3\epsilon\epsilon_0 NN_p\omega(R_\omega)^6 exp\left(\frac{e^2}{4\pi\epsilon\varepsilon_0 K_BT_gR_\omega}\right) \quad (7)$$

The hopping distance R_ω for the condition $\omega\tau$=1 is given by:

Table 4. Frequency Dependence of Activation Energy of a.c. Conduction (E_{ac}) in a-$Se_{80}Te_{10}Sb_{10}$ Alloy before and after Laser Exposure

Frequency (kHz)	Unexposed Sample E_{ac} (eV)	Exposed Sample E_{ac} (eV)
0.5	0.32	0.35
1	0.31	0.32
2	0.32	0.30
5	0.29	0.24
10	0.23	0.18

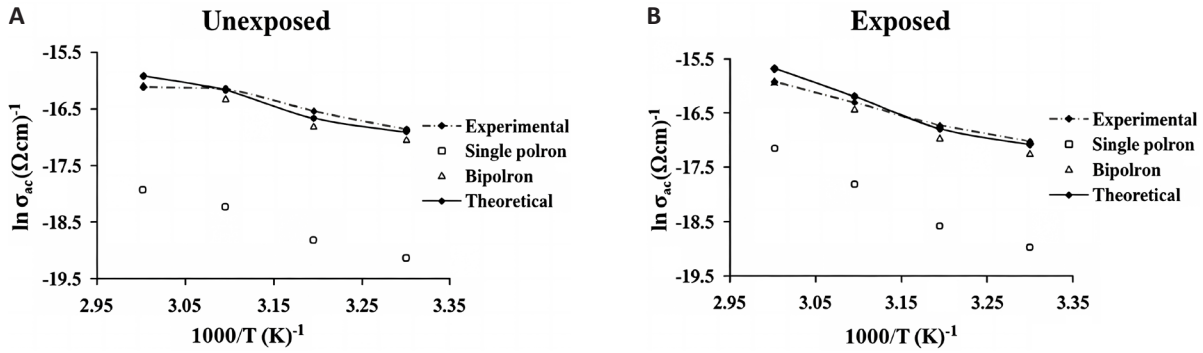

Figure 8. Comparative Analysis of Theoretical and Experimental a.c. Conductivity for Unexposed and Laser-Exposed Samples of a-$Se_{80}Te_{10}Sb_{10}$ Alloy.

Table 5. Density of Charged Defect States in a-$Se_{80}Te_{10}Sb_{10}$ Alloy before and after Laser Exposure

Sample	N (cm^{-3})
Unexposed sample	4.0×10^{21}
Exposed sample	1.7×10^{22}

$$R_\omega = \frac{2e^2}{\pi\epsilon\epsilon_0 W_m}\left[1+\frac{K_B T}{W_m} ln\,(\omega\tau_0)\right]^{-1} \quad (8)$$

The a.c. conductivity, $\sigma_{ac}(\omega)$, for single polaron hopping originating from randomly distributed defect centers can be expressed as[38]:

$$\sigma_{ac}(\omega) = \frac{1}{6}\pi^3 \varepsilon\varepsilon_0 N N_p \omega (R_\omega)^6 \quad (9)$$

Here, we have:

$$R_\omega = \frac{e^2}{\pi\varepsilon\varepsilon_0 W_m}\left[1+\frac{K_B T}{W_m} ln(\omega\tau_0)\right]^{-1} \quad (10)$$

Generally, a.c. conductivity of the chalcogenide glasses can be expressed as:

$$\sigma_{ac}(\omega) = [\sigma_{ac}(\omega)]_{single-polaron} + [\sigma_{ac}(\omega)]_{bipolaron} \quad (11)$$

Figure 8 compares the experimentally measured ac conductivity with the theoretical contributions from single-polaron hopping, bipolaron hopping, and their combined response for both the unexposed and laser-exposed samples at 1kHz. The calculated curves reproduce the experimental behaviour reasonably well, indicating that the CBH model is the dominant conduction mechanism in the present samples. It is evident that the bipolaron hopping component makes the major contribution to the total ac conductivity, whereas the single-polaron contribution remains comparatively small over the investigated temperature range. The laser irradiation increases the concentration of charged defect states in the present alloy (Table 5), consistent with the laser-induced structural rearrangement and partial crystallization revealed by the XRD, TEM, and Raman analyses.

3.4 Dielectric Relaxation

The dielectric response of the material is described by the complex dielectric function, which consists of a real component (ε′) representing the dielectric constant and an imaginary component (ε′′) corresponding to dielectric loss. The values of ε′ and ε′′ were calculated from the experimentally measured capacitance and dissipation factor over the frequency range of 0.5-100kHz and the temperature interval of 300-335K.

The variation of the dielectric constant with frequency for the unexposed and laser-exposed samples is presented in Figure 9A. Both samples exhibit pronounced frequency dispersion, particularly in the low-frequency region, where ε′ decreases rapidly with increasing frequency. A comparison of the two samples shows that laser irradiation consistently increases ε′ throughout the investigated temperature range. This enhancement is attributed to laser-induced structural relaxation and partial crystallization, which improve medium-range structural ordering and increase the polarizability of the glass network. The resulting reduction in structural disorder facilitates more effective dipolar and interfacial polarization under an applied electric field.

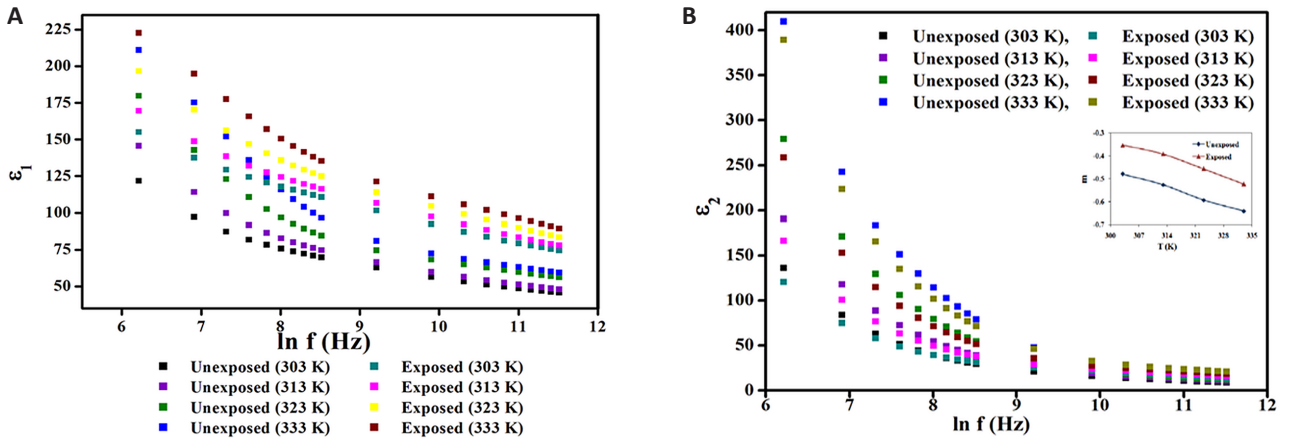

Figure 9. Frequency Dependence of Dielectric Constant (A) and Loss (B) for Unexposed and Laser-Exposed Samples of a-$Se_{80}Te_{10}Sb_{10}$ Alloy. A: Variation of the dielectric constant (epsilon_1) with ln(f) for the unexposed and exposed alloy at 303, 313, 323 and 333 K. B: Variation of the dielectric loss (epsilon_2) with ln(f) for the unexposed and exposed alloy at 303-333 K; the inset shows the exponent m as a function of temperature.

The dielectric behaviour can be interpreted using the Maxwell-Wagner interfacial polarization model together with Koops' theory[39]. According to this model, the material consists of relatively conducting grains separated by highly resistive grain boundaries. At low frequencies, mobile charge carriers accumulate at these interfaces, giving rise to significant space-charge polarization and consequently a large dielectric constant. As the applied frequency increases, the charge carriers can no longer respond rapidly to the alternating electric field, reducing interfacial polarization and causing the dielectric constant to decrease. At sufficiently high frequencies, the dielectric response is governed mainly by the grains, resulting in comparatively lower values of ε′. The continuous decrease in the dielectric constant with increasing frequency therefore reflects the electrical relaxation processes occurring within the material. The laser exposure increases the ε′ values while simultaneously reducing the dielectric loss over the investigated frequency range. The increase in ε′ is attributed to laser-induced structural relaxation and partial crystallization, which improve medium-range ordering and enhance the polarizability of the glass network. The growth of crystalline regions and reduction in structural disorder facilitate more effective dipolar and interfacial polarization under an applied electric field. In contrast, the reduction in dielectric loss suggests suppression of defect-assisted relaxation and charge-carrying centers responsible for energy dissipation. Laser-induced structural ordering decreases the density of weak bonds and metastable defect states, thereby reducing polarization losses and improving dielectric performance. Similar behaviour has been reported for structurally relaxed and partially crystallized chalcogenide glasses and phase-change materials, where enhanced ordering increases polarization while reducing dielectric dissipation[40].

The laser-exposed alloy consistently shows lower dielectric loss than the unexposed sample over the investigated frequency range, indicating that laser irradiation suppresses energy dissipation during dielectric polarization (Figure 9B). At higher frequencies, the dielectric loss becomes nearly frequency-independent, suggesting that the contribution of interfacial polarization becomes insignificant. The observed behaviour can be explained on the basis of the Maxwell-Wagner interfacial polarization mechanism. At low frequencies, charge carriers accumulate at interfaces between relatively conductive crystalline regions and the surrounding resistive amorphous matrix, giving rise to pronounced space-charge polarization and, consequently, higher dielectric loss. As the frequency increases, the localized charge carriers are unable to follow the rapidly alternating electric field, thereby reducing interfacial polarization and energy dissipation. Furthermore, laser-induced structural relaxation and partial crystallization reduce weakly bonded atomic configurations, leading to lower dielectric loss in the laser-exposed alloy. This observation is consistent with the XRD, TEM and Raman results, which collectively indicate improved structural ordering after laser irradiation.

Comparatively lower dielectric loss observed after laser irradiation further supports the occurrence of structural relaxation within the amorphous matrix. The reduction in weak-bond disorder and shallow trap states decreases the probability of defect-assisted hopping and interfacial charge accumulation, thereby reducing energy dissipation during polarization. This observation is consistent with the XRD, TEM and Raman results, which collectively indicate that laser irradiation promotes partial crystallization and improved structural ordering in the $Se_{80}Te_{10}Sb_{10}$ alloy.

According to model proposed by Giuntini et al.[41], dielectric loss (ε_2) at a particular frequency, in the temperature range where dielectric dispersion occurs, is expressed by:

$$\varepsilon_2 = (\varepsilon_s - \varepsilon_\infty) 2\pi^2 N (ne^2/\varepsilon_s)^3 k_B T \tau_0^m W_m^{-4} \omega^m \quad (12)$$

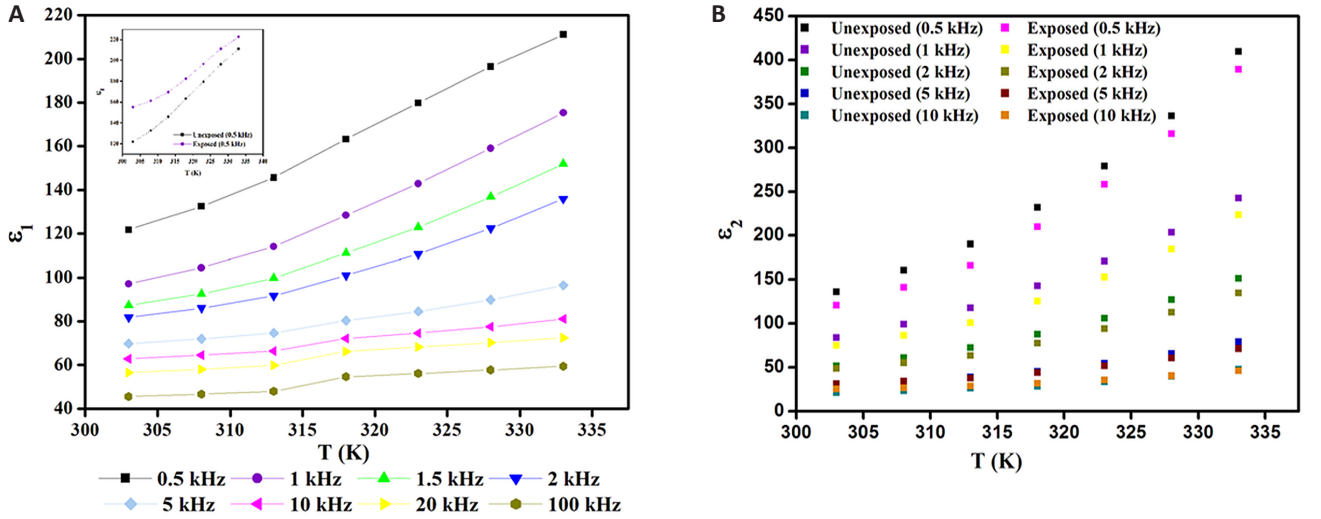

Figure 10. Temperature Dependence of Dielectric Constant (A) and Loss (B) for Unexposed and Laser-Exposed a-$Se_{80}Te_{10}Sb_{10}$ Alloy. A: Variation of the dielectric constant (epsilon_1) with temperature at 0.5, 1, 1.5, 2, 5, 10, 20 and 100kHz; the inset compares the unexposed and exposed alloy at 0.5 kHz. B: Variation of the dielectric loss (epsilon_2) with temperature for the unexposed and exposed alloy at 0.5, 1, 2, 5 and 10kHz.

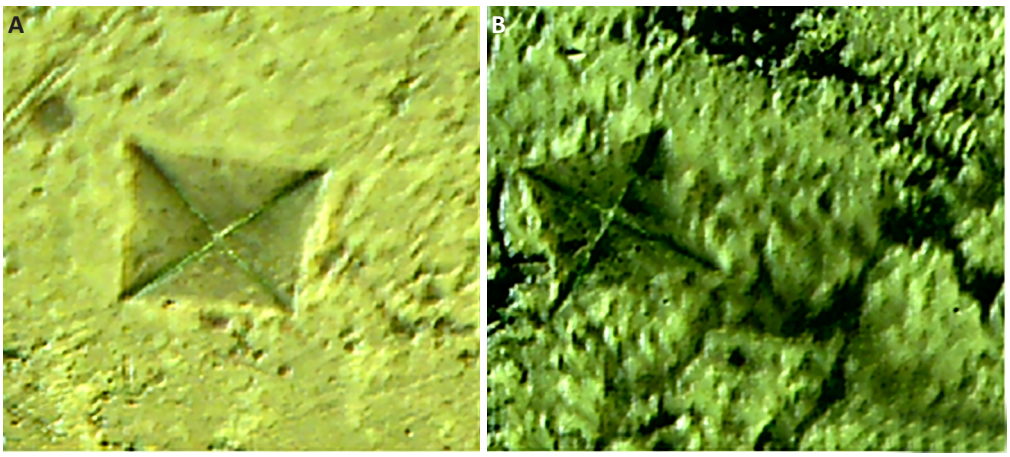

Figure 11. Impression of the Vickers Indentation on Polished Samples of (A) Unexposed and (B) Exposed a-$Se_{80}Te_{10}Sb_{10}$ Alloy.

Here, "*m*" is a power of angular frequency (ω) and is given by:

$$m = -\frac{4k_B T}{W_m} \quad (13)$$

Figure 10 shows that the calculated values of the frequency exponent m decrease as temperature increases, which suggests that the Debye model could not explain the overall dielectric relaxation.

The temperature dependence of the dielectric constant (ε′) measured at different frequencies is presented in Figure 10A, which shows the rise in ε′ for both virgin and laser-treated samples. The variation of ε′ at 0.5 kHz is compared in the inset of Figure 10A, where temperature has a particularly strong effect. In contrast, the temperature dependence weakens considerably at higher frequencies because the dipoles cannot follow the rapidly alternating electric field. The rise in ε′ with increasing *T* can be explained by greater thermal activation of localized charge carriers and orientable dipoles embedded in the amorphous glass matrix, thereby enhancing the material's overall polarization. As the temperature rises, charge carriers gain sufficient energy to overcome localized potential barriers, leading to improved dipolar orientation and stronger interfacial polarization. Consequently, the material's overall polarizability increases, leading to higher ε′ values. The laser-exposed sample exhibits a consistently higher ε′ than the unexposed alloy, which may be attributed to laser-induced structural relaxation and partial crystallization, thereby enhancing medium-range ordering and facilitating polarization. Figure 10B shows the corresponding variation of the dielectric loss (ε′′) with temperature at different frequencies. As with the dielectric constant, the dielectric loss increases gradually with temperature for both samples. The increase in ε′′ is primarily associated with thermally activated charge transport and enhanced dipolar relaxation. As the temperature increases, localized charge carriers become more mobile, promoting hopping between defect states and increasing electrical conduction.

Table 6. Thermo-mechanical Parameters (T_g, H_v, V_h, E_h, E) of a-$Se_{80}Te_{10}Sb_{10}$ Alloy before and after Laser Exposure

Thermo-Mechanical Parameters	Unexposed Sample	Exposed Sample
T_g (K)	339	343
H_V (Kgf/mm^2)	48.7	46.5
V_h (Å^3)	34.8	37.3
E_h (kJ/mol)	10.0	10.2
E (kgf/mm^2)	730.5	697.5

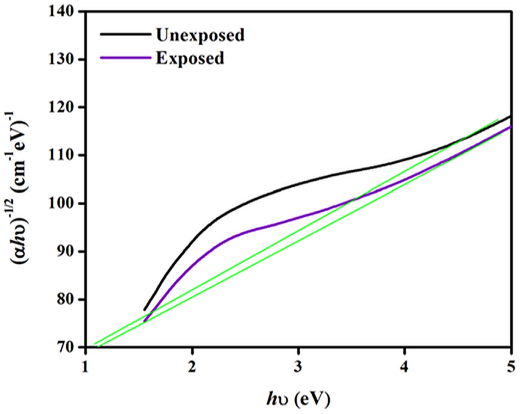

Figure 12. Plots of $(\alpha h\upsilon)^{1/2}$ versus Photon Energy ($h\upsilon$) for a-$Se_{80}Te_{10}Sb_{10}$ Alloy.

Simultaneously, thermal activation facilitates interfacial (space-charge) polarization, which contributes to additional energy dissipation during polarization. Consequently, a larger fraction of the applied electrical energy is converted into heat, increasing dielectric loss. These observations are consistent with the thermally activated dielectric behaviour commonly reported for amorphous chalcogenide glasses[42,43].

3.5 Thermo-mechanical Parameters

Figure 11A and B show micro-indentation imprints on the samples' surfaces at a load of 200g. The indenter mark was observed using computer-operated software to determine Vickers hardness. Ten individual measurements were made on both alloys, and the alloys were examined optically. After the indentation load was removed, the hardness (H_v) was measured, and the mean hardness value was determined. Using the experimental values of micro-hardness (H_v) from the hardness tester and glass transition temperature (T_g) from the differential scanning calorimeter, the values of other thermo-mechanical parameters, such as modulus of elasticity (E), the minimum volume of micro-voids (V_h) and the energy of their creation (E_h), have been calculated using the following relations:

$$E=15H_v \quad (14)$$

$$V_h = 3.58\ K_B \frac{T_g}{H_V} \quad (15)$$

$$E_h=3.58\ K_B T_g \quad (16)$$

The micro-hardness values and other related thermo-mechanical parameters are summarized in Table 6 for both samples. From this table, one can see that there are few changes in thermo-mechanical parameters after laser exposure.

3.6 Spectroscopic Measurement

3.6.1 Analysis of Absorption Edge and Optical Band Gap

The optical absorption behaviour in the high-absorption region ($\alpha \geq 10^4 cm^{-1}$) was analysed using the Tauc formalism for indirect electronic transitions. According to this model, the absorption coefficient is related to the photon energy as follows[44]:

$$\alpha h\upsilon = B\left(h\upsilon - E_{opt}\right)^2 \quad (17)$$

Here, E_{opt} is the Tauc optical band gap, $\alpha = 2.303\ A/d$ (A: optical density, d: the thickness of the samples), B is a constant that depends on the electronic transition probability, which is expressed as[45]:

$$B = \frac{(4\pi/c)\sigma_0}{n_0 \Delta E} \quad (18)$$

Here, n_0 is the static refractive index, ΔE is the localized-state tail width, c is the speed of light in vacuum, and σ_0 is the minimum metallic conductivity.

Figure 12 shows plots of $(\alpha h\upsilon)^{1/2}$ versus $h\upsilon$ in eV units for both samples. By extrapolating the linear portion of the curves to zero absorption, the indirect band gaps obtained from these plots are 1.08eV and 1.21eV for unexposed and exposed alloy, respectively.

This increase in the band gap can be attributed to the increase in the extent of the crystalline fraction within the amorphous matrix, resulting from a structural transformation from short-range order to medium-range order. The increase in the optical band gap is also consistent with reduced band-tail disorder enhanced structural ordering following laser-induced partial crystallization, thereby decreasing the density of localized states within the mobility gap. During laser irradiation, amorphous solids receive sufficient vibrational energy to break some weaker bonds, thereby introducing translational degrees of freedom into the system. Nasir and Zulfequar[46] have also observed a similar result.

3.6.2 Raman and IR Spectroscopic Analysis

We performed Raman spectroscopy measurements

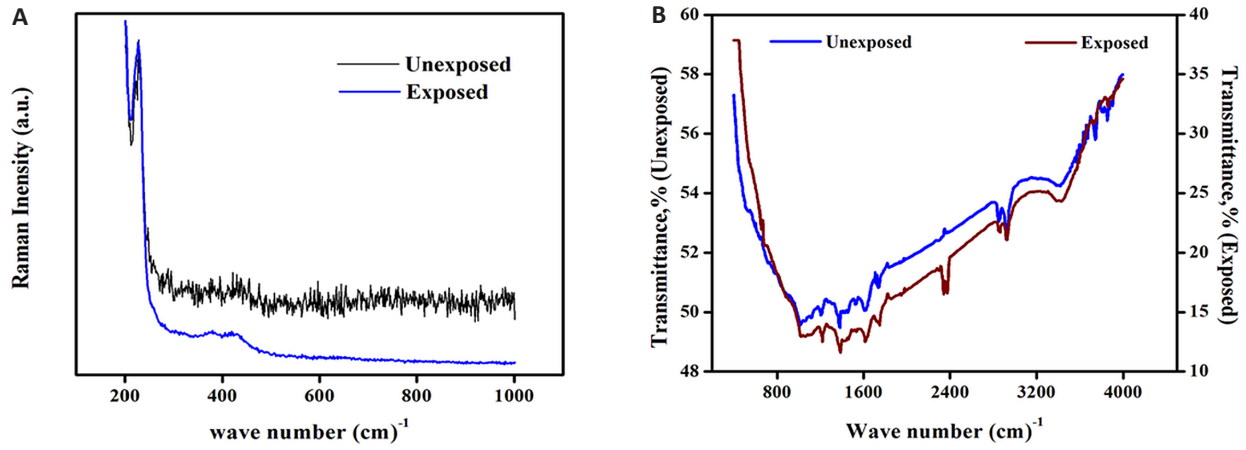

Figure 13. Raman (A) and FT-IR Transmission (B) Spectra of a-$Se_{80}Te_{10}Sb_{10}$ Alloy. A: Raman spectra of the unexposed and exposed alloy recorded over 200-1000 cm^{-1}. B: FTIR transmittance spectra of the unexposed and exposed alloy; the left axis refers to the unexposed and the right axis to the exposed sample.

Table 7. Mode of Vibration (in cm^{-1}) Before and After Laser Irradiation in a-$Se_{80}Te_{10}Sb_{10}$ Alloy

Unexposed Sample	Exposed Sample
1218.7	----
1613.5	1636.8
2852.3	2856.1
2923.9	2925.8

here to investigate how the Raman shift changes under laser exposure to the parent alloy, which affects the lattice structure. The Raman spectra of the unexposed and exposed a-$Se_{80}Te_{10}Sb_{10}$ alloy in the wavenumber range 200-1000cm^{-1} at room temperature are shown in Figure 13A. There is only one characteristic peak within the scanned frequency range in both alloys. In the unexposed a-$Se_{80}Te_{10}Sb_{10}$ alloy, the 228cm^{-1} peak is assigned to the Te_4 modes[46], while another peak (226cm^{-1}) corresponds to the Te_4 modes[46] and/or t-Se[47] in the laser-exposed sample. The slight shift in the Raman peak position after laser irradiation indicates a modification in the local bonding environment and short-range atomic arrangement within the glass network. The corresponding improvement in structural ordering is consistent with the XRD and TEM observations, which reveal grain growth and partial crystallization of the amorphous matrix following laser exposure. Thus, the Raman results provide additional evidence that He-Ne laser irradiation promotes structural rearrangement in the $Se_{80}Te_{10}Sb_{10}$ alloy.

The Raman observations are also consistent with recent reports demonstrating that laser irradiation induces subtle bond rearrangement and medium-range structural ordering in chalcogenide glasses prior to complete crystallization. Such structural evolution contributes to simultaneous modification of the optical band gap, electrical transport and dielectric response, thereby highlighting the effectiveness of laser processing as a non-contact approach for tuning multifunctional properties[48,49].

The FT-IR transmittance profiles recorded in the present study show distinct absorption features (Figure 13B). Following laser exposure, noticeable shifts in the vibrational band positions are evident, particularly for the modes initially at 1383.4, 1613.5, 1745.2, 2852.3, and 2923.9 cm^{-1}. Among these, the absorption peak centered at 2923.9cm^{-1} exhibits the highest intensity in the untreated specimen, whereas the corresponding stretching vibration observed at 2925.8cm^{-1} after laser treatment becomes comparatively weaker. The absorption bands near 1613 cm^{-1} in the pristine alloy and 1636.1 cm^{-1} in the irradiated counterpart are attributed to the bending vibration of H_2O molecules, most likely originating from atmospheric moisture absorbed during FT-IR sample handling and pellet preparation. A complete summary of the vibrational frequencies identified for both the untreated and laser-irradiated specimens is provided in Table 7.

All frequency bands 1383.4, 1613.5, 1745.2, 2852.3 and 2923.9 cm^{-1} are shifted from their positions after laser treatment. The band at 2923.9 cm^{-1} is remarkably intense in the untreated sample, whereas the stretching mode at 2925.8 cm^{-1} is less intense in the laser-treated sample. The bands at 1613 cm^{-1} and 1636.1 cm^{-1} are assigned to the H2O bending mode in both the as-synthesized and laser-exposed samples; this is likely due to moisture present during FT-IR sample preparation.

4 CONCLUSION

The controlled He-Ne laser irradiation induces partial crystallization in amorphous $Se_{80}Te_{10}Sb_{10}$ glass, resulting in significant modifications of its structural, dielectric, electrical and optical properties. XRD, TEM, and SEM consistently reveal grain growth and enhanced crystallinity, while DSC confirms changes in glass-transition behavior due to structural relaxation. Laser irradiation increases the dielectric constant and optical band gap while reducing dielectric loss, and modifies the electrical transport mechanism by altering localized defect states. These findings demonstrate that laser processing

offers an efficient, non-contact route for tailoring the functional properties of Se-Te-Sb glasses. The approach may be useful for the development of phase-change memories, optical recording media, integrated photonic devices and laser-written functional structures.

Acknowledgements

Not applicable.

Conflicts of Interest

The authors declared no conflict of interest.

Data Availability

The data that support the findings of this study are available from the corresponding author upon reasonable request.

Author Contribution

Chandel N performed the experiments, wrote original manuscript. Mehta N contributed to supervision and conceptualization, reviewed and edited manuscript.

Abbreviation List

CBH, Correlated barrier hopping
CCD, Charge-coupled device
DSC, Differential scanning calorimetry
FT-IR, Fourier-transform infrared
LCR, Inductance–capacitance–resistance
LPT, Large-polaron tunnelling
MDSC, Modulated differential scanning calorimetry
NIR, Near-infrared
NSPT, Non-overlapping small-polaron tunnelling
QMT, Quantum-mechanical tunnelling
SAED, Selected-area electron diffraction
SEM, Scanning electron microscopy
TEM, Transmission electron microscopy
UV-Vis, Ultraviolet–visible
XRD, X-ray diffraction

References

[1] Aly KA, Osman MA, Abousehly AM et al. Effect of heat treatment on the optical and electrical transport properties of $Ge_{15}Sb_{10}Se_{75}$ and $Ge_{25}Sb_{10}Se_{65}$ thin films. *J Phys Chem Solids*, 2008; 69: 2514-2519.[DOI]

[2] Zhu W, Wang C, Sun M et al. Effect of periodic number of $[Si/Sb_{80}Te_{20}]_x$ multilayer film on its laser-induced crystallization studied by coherent phonon spectroscopy. *Nanoscale Res Lett*, 2012; 7: 638.[DOI]

[3] Sivakumaran K, Shashidharan Nair CK. Rapid synthesis of chalcogenide glasses of Se-Te-Sb system by microwave irradiation. *J Phys D: Appl Phys*, 2005; 38: 2476-2479.[DOI]

[4] Efthimiopoulos I, Zhang J, Kucway M et al. Sb_2Se_3 under pressure. *Sci Rep*, 2013; 3: 2665.[DOI]

[5] Ivan I, Szegedi S, Daroczi L et al. Deuteron irradiation induced changes in amorphous AsSe films. *Nucl Instrum Methods Phys Res B*, 2005; 229: 240-245.[DOI]

[6] Balboul MR. Optical effects induced by gamma and UV irradiation in chalcogenic glass. *Radiat Meas*, 2008; 43: 1360-1364.[DOI]

[7] Amin GAM. γ-Irradiation effects on the optical properties of amorphous $Ge_{10}As_{30}Se_{60}$ thin films. *Nucl Instrum Methods Phys Res B*, 2009; 267: 3333-3336.[DOI]

[8] Yannopoulos SN, Siokou A, Nasikas NK et al. CO_2-laser-induced growth of epitaxial graphene on 6H-SiC (0001). *Adv Funct Mater*, 2012; 22: 113-120.[DOI]

[9] Cao S, Pedraza AJ, Allard LF. Laser-induced microstructural changes and decomposition of aluminum nitride. *J Mater Res*, 1995; 10: 54-62.[DOI]

[10] Kumar A, Shukla RK, Kumar A, Gupta R. Light-induced effects & defects in chalcogenide glassy semiconductors: A review. *Infrared Phys Technol*, 2019; 102: 103056.[DOI]

[11] Kang M, Sohn BU, Du Q et al. Self-healing mechanisms for Ge-Sb-S chalcogenide glasses upon gamma irradiation. *MRS Bull*, 2024; 49: 778-786.[DOI]

[12] El-Nahass MM, Ali MH, Moqbel MS et al. Photo-induced tuning of nonlinear near-infrared optical characteristics in $Ge_5Se_{80}In_{15}$ thin films. *Appl Phys A*, 2026; 132: 403.[DOI]

[13] Kutálek P, Samsonova E, Smolík J et al. Local photo-induced crystallization of Ge-Sb-Se bulk glasses by laser direct writing. *Ceram Int*, 2026; 52: 5592-5602.[DOI]

[14] Tanka K. The Photoexpansion in Chalcogenide Glasses: Excitonic Effects in S/Se Chains and Rings. *Phys Status Solidi B*, 2026; 263: e70172.[DOI]

[15] Kang M, Sharma R, Blanco C et al. Solution-derived Ge-Sb-Se-Te phase-change chalcogenide films. *Sci Rep*, 2024; 14: 18151.[DOI]

[16] Yang Z, Zhang Z, Lin Y et al. High index-contrast GeSbSe chalcogenide waveguide for integrated nonlinear photonics. *Opt Mater Express*, 2025; 15: 1224-1235.[DOI]

[17] Khan SA, Zulfequar M, Husain M. Laser-induced amorphization and crystallization on $Se_{80}Te_{20-x}Pb_x$ thin films. *Vacuum*, 2004; 72: 291-296.[DOI]

[18] Das S, Senapati S, Alagarasan D et al. Laser-induced modification in structural, morphological, linear and non-linear optical parameters of $Ge_{20}Ag_{10}Te_{10}Se_{60}$ thin films for optoelectronic applications. *Mater Sci Semicond Process*, 2023; 160: 107456.[DOI]

[19] Liu J, Chen Z, Wu C et al. Recent Advances in Antimony Selenide Photodetectors. *Adv Mater*, 2024; 36: e2406028.[DOI]

[20] Barthwal S, Kumar R, Pathak S. Present Status and Future Perspective of Antimony Chalcogenide (Sb_2X_3) Photovoltaics. *ACS Appl Energy Mater*, 2022; 5: 6545-6585.[DOI]

[21] Chen G, Chen S, Zhao J et al. Advances in optoelectronic applications of antimony chalcogenide thin films. *Nano Res*, 2025; 18: 94907931.[DOI]

[22] Virt IS, Rudyj IO, Kurilo IV et al. Properties of Sb_2S_3 and Sb_2Se_3 thin films obtained by pulsed laser ablation. *Semiconductors*, 2013; 47: 1003-1007.[DOI]

[23] Xue MZ, Fu ZW. Pulsed laser deposited Sb_2Se_3 anode for lithium-ion batteries. *J Alloys Compd*, 2008; 458: 351-356.[DOI]

[24] Rodriguez-Lazcano Y, Peña Y, Nair MTS et al. Polycrystalline thin films of antimony selenide via chemical bath deposition and post deposition treatments. *Thin Solid Films*, 2005; 493: 77-82.[DOI]

[25] El-Sayad EA. Compositional dependence of the optical properties of amorphous $Sb_2Se_{3-x}S_x$ thin films. *J Non-Cryst Solids*, 2008; 354: 3806-3810.[DOI]

[26] Bendt G, Zastrow S, Nielsch K et al. Deposition of topological insulator Sb_2Te_3 films by an MOCVD process. *J Mater Chem A*, 2014; 2: 8215-8222.[DOI]

[27] Hao G, Qi X, Wang G et al. Synthesis and characterization of few-layer Sb_2Te_3 nanoplates with electrostatic properties. *RSC Adv*, 2012; 2: 10694-10700.[DOI]

[28] Zastrow S, Gooth J, Boehnert T et al. Thermoelectric transport and Hall measurements of low defect Sb_2Te_3 thin films grown by atomic layer deposition. *Semicond Sci Technol*, 2013; 28: 035010.[DOI]

[29] Tripathi SK, Sharma V, Thakur A et al. Effect of Sb additive on the electrical properties of Se-Te alloy. *J Non-Cryst Solids*, 2005; 351: 2468-2473.[DOI]

[30] Holzwarth U, Gibson N. The Scherrer equation versus the 'Debye-Scherrer equation'. *Nat Nanotechnol*, 2011; 6: 534.[DOI]

[31] Lebedeva YS, Smayev M, Budagovsky IA et al. Photoinduced crystallization of Sb_2Se_3 and $Ge_2Sb_2Te_5$ chalcogenide films. *J Surf Investig*, 2023; 17: 339-348.[DOI]

[32] Giri S, Kumar PC, Supriya S et al. Enhanced photodetectivity and responsivity in $In_{10}Se_{70}Te_{15}Bi_5$ film by time-dependent laser irradiation for photodetector applications. *RSC Adv*, 2025; 15: 46821-46837.[DOI]

[33] Kauzmann W. The nature of the glassy state and the behavior of liquids at low temperatures. *Chem Rev*, 1948; 43: 219-256.[DOI]

[34] Hrubý A. Evaluation of glass-forming tendency by means of DTA. *Czech J Phys B*, 1972; 22: 1187-1193.[DOI]

[35] Pollak M, Geballe TH. Low-frequency conductivity due to hopping processes in silicon. *Phys Rev*, 1961; 122: 1742-1753.[DOI]

[36] Ghosh A. Frequency-dependent conductivity in bismuth-vanadate glassy semiconductors. *Phys Rev B*, 1990; 41: 1479-1488.[DOI]

[37] Elliott SR. Temperature dependence of a.c. conductivity of chalcogenide glasses. *Philos Mag B*, 1978; 37: 553-560.[DOI]

[38] Elliott SR. A.c. conduction in amorphous chalcogenide and pnictide semiconductors. *Adv Phys*, 1987; 36: 135-217.[DOI]

[39] Koops CG. On the dispersion of resistivity and dielectric constant of some semiconductors at audio frequencies. *Phys Rev*, 1951; 83: 121-124.[DOI]

[40] Kumar A, Mehta N. Laser-induced persistent photo-dielectric effects in Se-Te-Sn-Cd chalcogenide glassy semiconductors (STSC ChGs). *J Mater Chem C*, 2018; 6: 2747-2759.[DOI]

[41] Giuntini JC, Zanchetta JV, Jullien D et al. Temperature dependence of dielectric losses in chalcogenide glasses. *J Non-Cryst Solids*, 1981; 45: 57-62.[DOI]

[42] Anantharaman MR, Sindhu S, Jagatheesan S et al. Dielectric properties of rubber ferrite composites containing mixed ferrites. *J Phys D: Appl Phys*, 1999; 32: 1801-1807.[DOI]

[43] Stevels JM. Electrical Conductivity II. In: Flugge S (ed.). Handbuch der Physik (Encyclopedia of Physics). Springer: Berlin, 1957; 350-391.[DOI]

[44] Tauc J. Optical properties and electronic structure of amorphous Ge and Si. *Mater Res Bull*, 1974; 159-220.[DOI]

[45] Mott NF, Davis EA. Electronic Processes in Non-Crystalline Materials, 2nd ed. Clarendon Press: Oxford, UK, 1979.

[46] Hassanzadeh P, Thompson C, Andrews L. Absorption spectra of tellurium clusters in solid argon. *J Phys Chem*, 1992; 96: 8246-8249.[DOI]

[47] Lucovsky G, Mooradian A, Taylor W et al. Identification of the fundamental vibrational modes of trigonal, α-monoclinic and amorphous selenium. *Solid State Commun*, 1967; 5: 113-117.[DOI]

[48] Azhniuk YM, Gomonnai AV, Kryshenik VM et al. Raman study of photoinduced changes in Cd-doped amorphous $GeSe_2$ films. *Mater Today Proc*, 2022; 62: 5759-5762.[DOI]

[49] Tsiulyanu D, Veres M, Holomb R et al. Raman scattering evidence on the correlation of middle range order and structural self-organization of As-S-Ge glasses in the intermediate phase region. *J Non-Cryst Solids*, 2023; 609: 122255.[DOI]